Journal of Volcanology and Geothermal Research 260 (2013) 43–51

Contents lists available at SciVerse ScienceDirect

Journal of Volcanology and Geothermal Research

journal homepage: www.elsevier.com/locate/jvolgeores

Dynamic deformation of Seguam Island, Alaska, 1992–2008, from multi-interferogram InSAR processing

Chang-Wook Lee [a], Zhong Lu [b,*], Joong-Sun Won [c], Hyung-Sup Jung [d], Daniel Dzurisin [b]

[a] National Institute of Meteorological Research, Korea Meteorological Administration, 45 Gisangcheong-gil, Sindaebang-dong, Dongjak-gu, Seoul 156-720, Republic of Korea
[b] U.S. Geological Survey, Cascades Volcano Observatory, Vancouver, WA 98683, USA
[c] Department of Earth System Sciences, Yonsei University, 134 Shinchon-dong, Seodaemun-gu, Seoul 120-749, Republic of Korea
[d] Department of Geo-Informatics, University of Seoul, 90 Jeonnong-dong, Dongdaemun-gu, Seoul, 130-743, Republic of Korea

ARTICLE INFO

Article history:
Received 19 February 2013
Accepted 7 May 2013
Available online 28 May 2013

Keywords:
InSAR
Time series
Deformation
Seguam

ABSTRACT

We generated a time-series of ERS-1/2 and ENVISAT interferometric synthetic aperture radar (InSAR) images to study ground surface deformation at Seguam Island from 1992 to 2008. We used the small baseline subset (SBAS) technique to reduce artifacts associated with baseline uncertainties and atmospheric delay anomalies, and processed images from two adjacent tracks to validate our results. Seguam Island comprises the remnants of two late Quaternary calderas, one in the western caldera of the island and one in the eastern part of the island. The western caldera subsided at a constant rate of ~1.6 cm/yr throughout the study period, while the eastern caldera experienced alternating periods of subsidence and uplift: ~5 cm/year uplift during January 1993–October 1993 (stage 1), ~1.6 cm/year subsidence during October 1993–November 1998 (stage 2), ~2.0 cm/year uplift during November 1998–September 2000 (stage 3), ~1.4 cm/year subsidence during September 2000–November 2005 (stage 4), and ~0.8 cm/year uplift during November 2005–July 2007 (stage 5). Source modeling indicates a deflationary source less than 2 km below sea level (BSL) beneath the western caldera and two sources beneath the eastern caldera: an inflationary source 2.5–6.0 km BSL and a deflationary source less than 2 km BSL. We suggest that uplift of the eastern caldera is driven by episodic intrusions of basaltic magma into a poroelastic reservoir 2.5–6.0 km BSL beneath the caldera. Cooling and degassing of the reservoir between intrusions result in steady subsidence of the overlying surface. Although we found no evidence of magma intrusion beneath the western caldera during the study period, it is the site (Pyre Peak) of all historical eruptions on the island and therefore cooling and degassing of intrusions presumably contributes to subsidence there as well. Another likely subsidence mechanism in the western caldera is thermoelastic contraction of lava flows emplaced near Pyre Peak during several historical eruptions, most recently in 1977 and 1992–93.

Published by Elsevier B.V.

1. Introduction

Seguam Island (Fig. 1), located in the central Aleutian arc, is approximately 170 km north of the Aleutian trench where the Pacific plate is subducting obliquely beneath the North American plate at a convergence rate of 6–7 cm/year (Jicha and Singer, 2006). Seguam rises above two of the largest basins (Amlia and Amukta basins) north of the Andreanof block, which is one of several segmented blocks along the arc that have undergone clockwise rotation accompanied by arc-parallel extension (Lu and Wyss, 1996; Jicha et al., 2004). The Amlia and Amukta basins define an arc-parallel graben structure beneath Seguam (Singer et al., 1992). The 200-km^2 island, which consists of Pleistocene–Recent tholeiitic lavas and tephras (Singer et al., 1992), hosts two collapse calderas and many satellite cones and vents. The eastern, 8-km-long, 4-km-wide caldera, was created by partial collapse about 9000 years ago of Wilcox Volcano, a 20 km^3 stratocone comprising mostly basaltic to rhyolitic lava flows. The western caldera is younger than eastern caldera and hosts Pyre Peak (a.k.a. Seguam Volcano), the site of at least 8 eruptions during the past two centuries (Miller et al., 1998; Jicha and Singer, 2006) (Fig. 1b). Seven major volcanic vents on Seguam Island are aligned in a roughly arc-parallel direction, congruent with arc-parallel faults in the Amlia and Amukta basins (Geist et al., 1987).

The earliest documented eruptive activity at Seguam occurred during 1786–90, followed by reported eruptions in 1827, 1891, 1892, 1901, and 1927 (Miller et al., 1998). The most recent eruptions occurred in March 1977 and intermittently from December 1992 through August 1993 (Masterlark and Lu, 2004). The 1977 eruption was a fissure eruption radiating southeastward from Pyre Peak to a vent with a 2.5 km distance (Price, 2004). The 1992–93 eruption comprised a series of intermittent eruptions that produced lava flows and tephra plumes from vents between Pyre Peak and the 1977 satellite cone (Miller et al., 1998).

* Corresponding author. Tel.: +1 360 993 8911; fax: +1 360 993 8981.
E-mail address: lu@usgs.gov (Z. Lu).

0377-0273/$ – see front matter. Published by Elsevier B.V.
http://dx.doi.org/10.1016/j.jvolgeores.2013.05.009

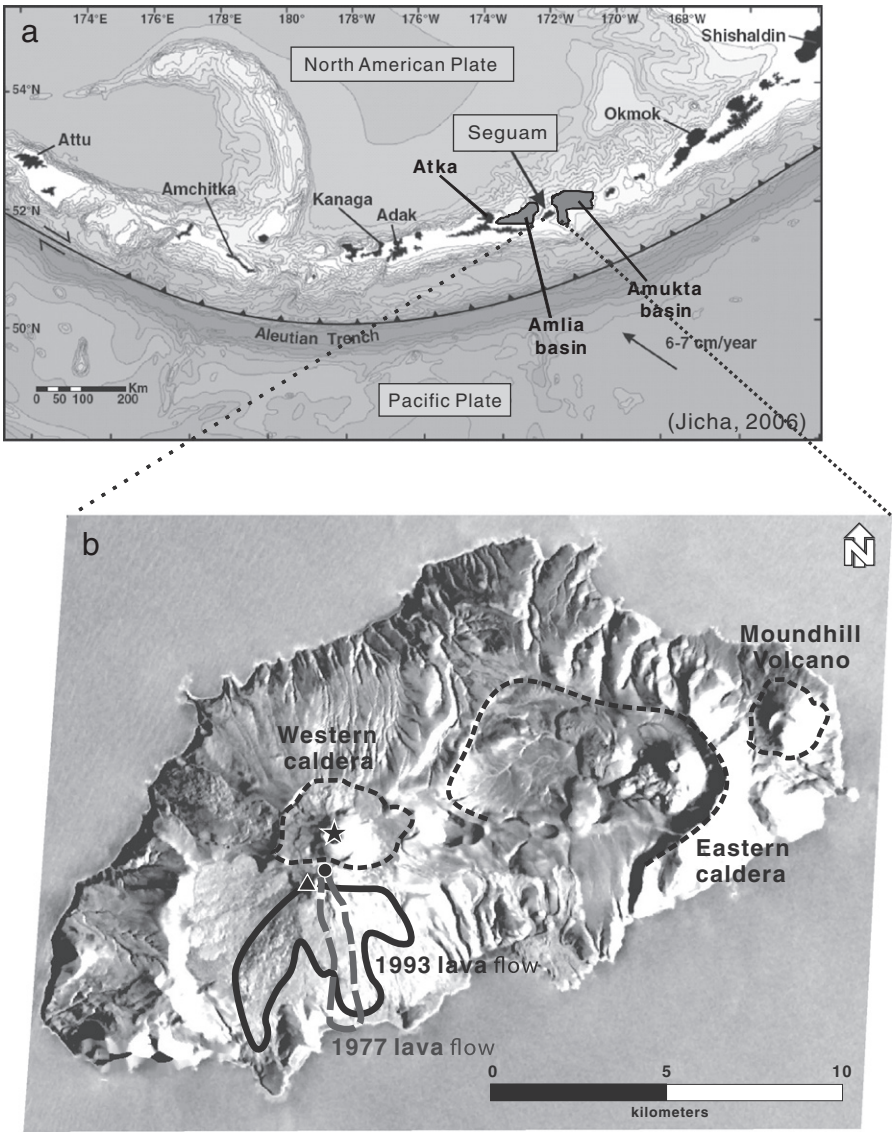

Fig. 1. (a) Seguam Island is located in the central Aleutian volcanic arc between the Amlia and Amukta tectonic basins. Also shown are the locations of several other islands (Attu, Amchitka, Kanaga, Ada, Atka) and volcanoes (Okmok, Shishaldin) in the Aleutian arc. (b) Seguam Island hosts two late Quaternary calderas. The eastern caldera formed by sector collapse of Wilcox Volcano about 9000 years ago. Moundhill Volcano is a postcollapse monogenetic basalt cone built on the eastern flank of Wilcox. The western caldera formed during an initial vent-clearing eruption that produced a 3.2 km^3 andesitic ignimbrite. The intracaldera cone Pyre Peak has been the site of all historical eruptions at Seguam, including the most recent in 1977 and 1992–93.

Interferometric synthetic aperture radar (InSAR) (Massonnet and Feigl, 1998; Ferretti et al., 2001; Berardino et al., 2002) is a proven technique for monitoring remote volcanoes such as Seguam. Deformation of Seguam Island was first observed with InSAR by Lu et al. (2003). Masterlark and Lu (2004) and Price (2004) independently studied deformation of Seguam using ERS-1/2 InSAR images acquired from 1992 to 2000. Masterlark and Lu (2004) used an array of Mogi (1958) point sources to model the deformation field, and Price (2004) used a smaller number of Mogi sources to model several representative interferograms. Neither study adequately addressed atmospheric delay anomalies and baseline-induced errors, which can produce significant artifacts in InSAR images.

For this paper, we processed all available ERS-1/2 and Envisat SAR images acquired from 1992 to 2008 to map surface deformation of Seguam Island and then modeled the observed deformation field using three different source geometries. Our study improves upon previous studies (Lu et al., 2003; Masterlark and Lu, 2004; Price, 2004) in several respects. First, we used an improved InSAR small baseline subset (SBAS) technique (Berardino et al., 2002; Lee et al., 2010) to produce a deformation time-series from all available useful interferograms. Our InSAR SBAS method takes into account atmospheric delay artifacts and DEM errors, uses an iterative approach to correct phase unwrapping errors, and includes additional temporal smoothing to suppress atmospheric delay anomalies (Schmidt and Burgmann, 2003). Second, we extended the time period of previous investigations from 1992–2000 to 1992–2008. Third, we processed radar images from two adjacent ERS-1/2 tracks and compared results to validate the deformation time-series. We also processed Envisat images acquired during 2004–08 along two adjacent tracks and compared the ERS-1/2 and Envisat results for additional verification. Fourth, we divided the deformation time-series during the study period into 5 distinct stages and modeled the average deformation signal for each stage using Mogi, sill, and ellipsoid source geometries. We used the deformation time-series and modeling results to infer the physical processes responsible for surface uplift and subsidence, and to develop a conceptual model of Seguam's magma storage and transport system.

2. InSAR analysis

2.1. Background of SBAS method

The SBAS algorithm was proposed by Berardino et al. (2002) to produce time-series records of surface deformation. This algorithm uses interferograms with small baselines that overlap in time in order to reduce spatial decorrelation, and to mitigate atmospheric artifacts and topographic errors in time-sequential interferometric pairs. The phase ($\Delta\phi$) of each interferogram baseline is defined by:

$$\Delta\phi(x,r)\approx\frac{4\pi}{\lambda}\left\{\Delta d(x,r)+\frac{B_{\perp}}{r\sin\theta}\Delta z(x,r)\right\}+\Delta\phi_{atmo}(x,r)+\Delta\phi_{n}(x,r), \quad (1)$$

where x and r are the azimuth and slant-range pixel coordinates, respectively, λ the radar wavelength, $B_{\perp}$ the perpendicular baseline, θ the SAR look angle, Δd the surface displacement in the radar look direction, Δz the topographic error, $\Delta\phi_{atmo}$ the atmospheric phase-delay artifact, and $\Delta\phi_{n}$ the phase due to other noise sources (Berardino et al., 2002). The SBAS method calculates the topographic error through the dependence of the interferogram phase on the perpendicular baseline. The technique estimates the atmospheric artifact using a spatial low-pass filter followed by a temporal high-pass filter, and then removes the atmospheric noise from the interferogram phase (Berardino et al., 2002).

Lee et al. (2010) refined the SBAS algorithm to allow for non-linear dependence of the deformation rate on time. Compared with the original SBAS algorithm, this method improves estimates of time-series deformation in four respects. First, phase unwrapping errors are corrected by distinguishing between high-quality (HQ) images in which no unwrapping errors could be found and low-quality (LQ) ones in which phase jumps due to unwrapping errors might exist. Phase unwrapping errors in the latter group can be corrected in the 2nd iteration of SBAS processing (Lu et al., 2010). Second, estimates of atmospheric artifacts, topographic errors, and time-series deformation measurements are refined through an iteration procedure. Third, temporal noise is further mitigated by the finite difference smoothing approach (Schmidt and Burgmann, 2003). Finally, procedures are implemented to correct any phase bias due to orbital and atmospheric phase artifacts at the reference point. This algorithm yields temporal surface deformation while minimizing atmospheric artifacts, DEM errors, and phase unwrapping errors (Lee et al., 2010).

2.2. SAR data

Seguam Island was imaged by ERS-1/2 and Envisat from two adjacent orbits, i.e., tracks 473 and 201. For this study, we obtained a total of 42 ERS-1/2 SAR images acquired from December 1992 to September 2008 along track 473 and 54 ERS-1/2 images acquired from January 1993 to September 2008 along track 201 (Table 1). We combined the images from each SAR to produce 135 interferograms from track 473 and 242 interferograms from track 201. We also obtained 16 ENVISAT images from track 201 and 14 images from track 473 (Table 1), from which we generated 22 and 23 interferograms (Fig. 2), respectively. C-band ERS-1/-2 and Envisat SAR images of Seguam maintain greater and more persistent coherence than for other Aleutian volcanoes, presumably because the percentage of lava flow coverage on Seguam is among the highest in the Aleutian arc (Lu et al., 2003). Coherence can be maintained for up to 10 years on parts of the island if the SAR images are acquired in summers and if the baseline of the InSAR pair is small. Coherence is generally higher in the western caldera of the island, including Pyre Peak, than in the eastern caldera. We used the Shuttle Radar Topography Mission (SRTM) 1-arc-second digital elevation model (DEM) to remove topographic effects from the interferograms. Relative and absolute vertical accuracies of SRTM DEMs are better than 10 m and 16 m, respectively (Farr et al., 2007). DEM errors of this magnitude would result in less than 6 mm error in line-of-sight (LOS) displacement measurements for the interferograms used in this study (Massonnet and Feigl, 1998).

Table 1
Acquisition dates of ERS and ENVISAT images (tracks 201 & 473) used for this study.

ERS-2 C-band (Descending mode)				ENVISAT C-band (Descending mode)	
(Track:201) Date		(Track:473) Date		(Track:201) Date	(Track:473) Date
1993-01-15	2002-08-05	1992-12-30	2003-10-18	2004-08-09	2004-06-19
1993-06-04	2002-09-09	1993-02-03	2004-06-19	2004-09-13	2004-08-28
1993-07-09	2002-10-14	1993-03-10	2004-08-28	2004-10-18	2004-10-02
1993-08-13	2002-12-23	1993-05-19	2004-10-02	2004-11-22	2005-07-09
1993-09-17	2003-01-27	1993-06-23	2005-06-04	2005-06-20	2005-09-17
1993-10-22	2003-03-03	1995-05-12	2005-07-09	2005-07-25	2005-10-22
1995-05-28	2003-06-16	1995-06-16	2006-07-29	2005-08-29	2006-06-24
1995-09-10	2003-07-21	1999-07-31	2006-09-02	2005-10-03	2006-07-29
1995-12-25	2003-08-25	1999-09-04	2006-10-07	2005-11-07	2006-09-02
1997-09-15	2003-09-29	1999-10-09	2007-06-09	2006-06-05	2006-10-07
1997-10-20	2003-11-03	1999-11-13	2007-07-14	2006-07-10	2007-06-09
1998-05-18	2004-05-31	2000-07-15	2007-09-22	2006-08-14	2008-06-28
1998-10-05	2004-07-05	2000-08-19	2007-10-27	2007-09-03	2008-08-02
1998-11-09	2004-09-13	2001-06-30	2008-06-28	2008-07-14	2008-09-06
1999-07-12	2004-10-18	2001-08-04	2008-09-06	2008-08-18	
1999-08-16	2005-07-25	2001-09-08		2008-09-22	
1999-09-20	2005-10-03	2001-10-13			
2000-05-22	2005-11-07	2002-07-20			
2000-06-26	2006-06-05	2002-08-24			
2000-07-31	2006-07-10	2002-09-28			
2000-09-04	2006-09-18	2002-11-02			
2000-11-13	2006-10-23	2003-02-15			
2001-07-16	2007-06-25	2003-03-22			
2001-08-20	2007-07-30	2003-04-26			
2001-09-24	2007-09-03	2003-07-05			
2001-10-29	2007-10-08	2003-08-09			
2002-07-01	2008-09-22	2003-09-13			

2.3. SBAS processing of ERS-1/-2 images

We used the refined SBAS method to measure time-series deformation at Seguam during 1992–2008 by analyzing a total of 48 and 28 HQ interferograms (Fig. 2) from tracks 201 and 473, respectively. There are no GPS or other ground-based geodetic measurements for comparison to the InSAR results, but we processed InSAR data from two adjacent tracks and compared the independent results for verification.

Fig. 3 shows maps of the average deformation rate at Seguam during 1992–2007. Images in Fig. 3a and b include all pixels regardless of their degree of coherence, whereas those in Fig. 3c and d include only

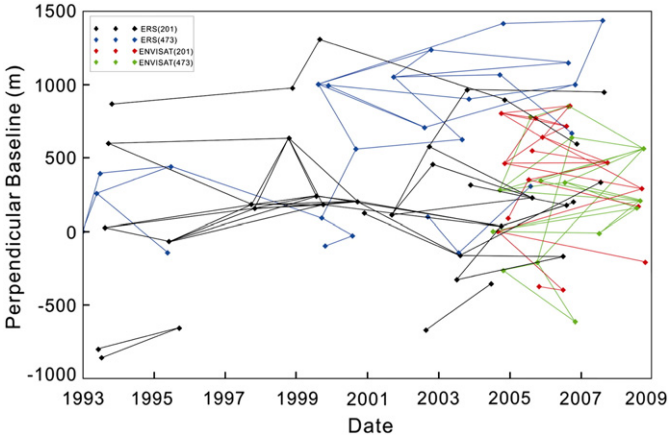

Fig. 2. Perpendicular baselines and time separations used for SBAS InSAR processing at Seguam Island from ERS and ENVISAT satellites for tracks 201 and 473, respectively.

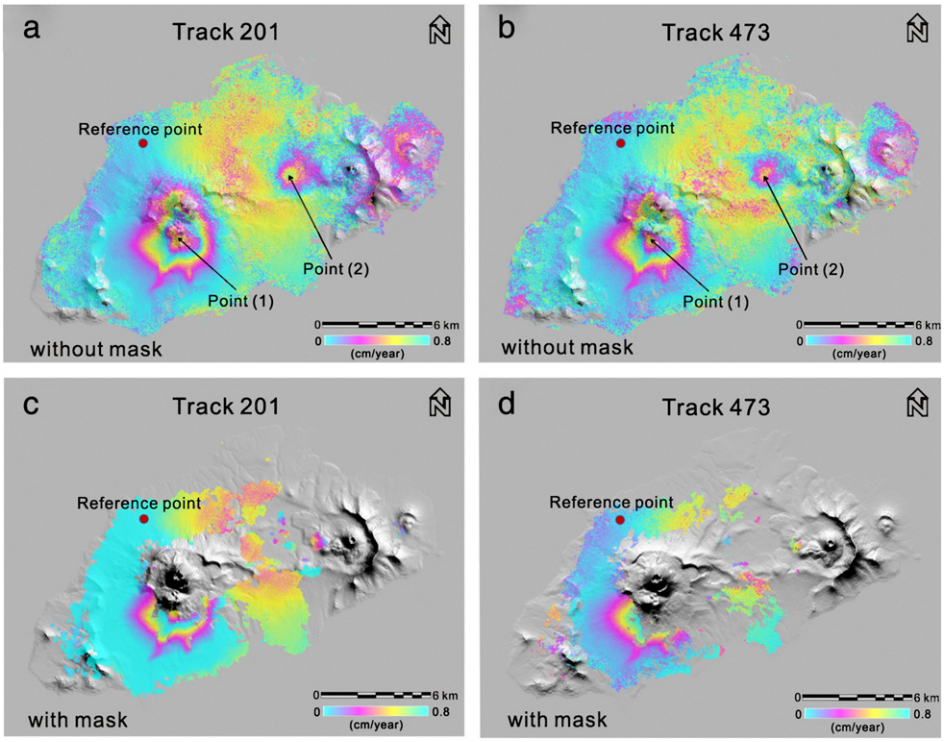

Fig. 3. Average line-of-sight surface displacement rate maps for Seguam from a refined SBAS processing technique for ERS-1/2 tracks 201 (a, c) and 473 (b, d). The images in 2a and 2b were processed using all pixels, whereas those in 2c and 2d were processed only for pixels that are coherent in all of the constituent interferograms. Essential features of the deformation field are the same in both versions. Red circle represents the reference point used for SBAS processing; see text for details. Time-series of line-of-sight surface displacement at points 1 and 2 are shown in Fig. 5.

pixels with coherence larger than 0.2. The estimated deformation rates with and without masking are essentially identical. We used the non-masked images for modeling as the results without masks (Fig. 3a and b) characterize the deformation field well and are more complete.

The look angle difference between tracks 201 and 473 is 1.7° and the average deformation rates obtained from two adjacent, independent ERS tracks agree with each other very well. This suggests that our SBAS procedure can suppress the artifacts (orbital, atmospheric and DEM errors) in the original InSAR images (Gonzalez and Fernandez, 2011; Manzo et al., 2012), and gives us confidence in the validity of the results. In general, the western half of Seguam showed steady subsidence centered near the 1977 and 1992–93 vents throughout the study period, while the eastern half showed episodic uplift alternating with subsidence.

2.4. SBAS processing of ENVISAT images

We processed Envisat images from tracks 201 and 473 that were acquired during 2004–08 and compared the results with those obtained from ERS-1/2 images. We used 16 and 14 ENVISAT images from tracks 201 and 473, respectively (Table 1), to generate 22 and 23 interferograms (Fig. 2), 17 and 11 of which are considered to be of high quality. For comparison, 11 and 10 ERS-1/2 images from tracks 201 and 473 yielded 11 and 8 interferograms, 6 and 5 of which are of high quality. Fig. 4 shows average deformation-rate maps produced from 4 independent sets of SBAS processing based on 2 tracks of Envisat and 2 tracks of ERS-1/2 interferograms, respectively. The two Envisat deformation-rate images agree both with each other and with the ERS-1/2 results, which further boosts our confidence in the results. Subtle differences in the deformation rate over the eastern caldera, ranging from −5 mm/year to 5 mm/year, are likely due to the limited numbers of interferograms used in the SBAS processing.

2.5. Time-series deformation

Fig. 5 shows time-series displacements at deformation centers in the western and eastern calderas of Seguam Island. A constant maximum subsidence rate of 1.6 cm/year can be found at point 1. Time-series analysis of the eastern caldera suggests that the 16-year investigation period can be divided into 5 stages (Fig. 6). This caldera inflated before and during the 1992–1993 eruption with an average rate of ~5 cm/yr (stage 1) from January 1993 to October 1993 (Fig. 6a). During stage 2 from October 1993 to November 1998 (Fig. 6d), subsidence occurred in both calderas at an average rate of ~1.6 cm/yr. The pattern changed during stage 3 from November 1998 to September 2000 (Fig. 6g), when uplift occurred at an average rate of ~2.0 cm/yr in the eastern caldera while subsidence continued in the western caldera. During stage 4 from September 2000 to November 2005 (Fig. 6j) the surface deformation pattern reverted to that of stage 2 (~1.4 cm/yr subsidence in both calderas), and during stage 5 from November 2005 to July 2007 (Fig. 6m) the pattern reverted to that of stage 3 (~0.8 cm/yr uplift in the eastern caldera, ~1.6 cm/yr subsidence in the western caldera). In other words, steady subsidence of both calderas was thrice interrupted by uplift episodes in the eastern caldera, even though the 1992–93 eruption that immediately preceded the study period occurred in the western caldera near Pyre Peak.

3. Deformation modeling

3.1. Mogi model

Our InSAR analysis identified two distinct deformation centers at Seguam (Fig. 6). The western center is located near the 1977 and 1992–93 vents and subsided at a nearly constant rate of ~1.6 cm/year, while the eastern center alternately subsided ~1.5 cm/year or rose 0.8–5 cm/yr. To investigate the sources responsible for these surface

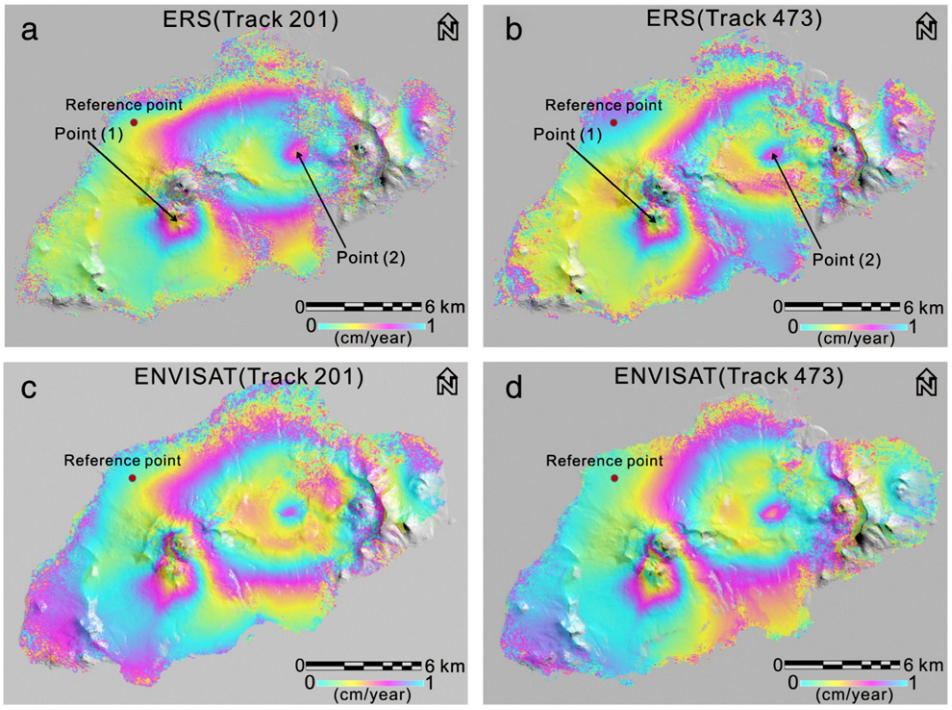

Fig. 4. Average line-of-sight surface displacement rate maps for Seguam during 2004–08 from independent SBAS processing of ERS-2 (a, b) and Envisat (c, d) SAR images acquired from tracks 201 (a, c) and 473 (b, d).

deformation patterns, we first modeled the average deformation-rate images for each of the five stages identified above using a point source in an elastic homogeneous half-space medium (Mogi, 1958). The point source approximation is valid if the size of the source dimension is much smaller than its depth. A limitation of the half-space formulation is the neglect of topographic effects. To account for topographic effects, we adopted a simple approach proposed by Williams and Wadge (1998), in which the elevation of the reference surface varies according to the elevation of each computation point in the model. Using a Mogi source located beneath each of the deformation centers, we obtained

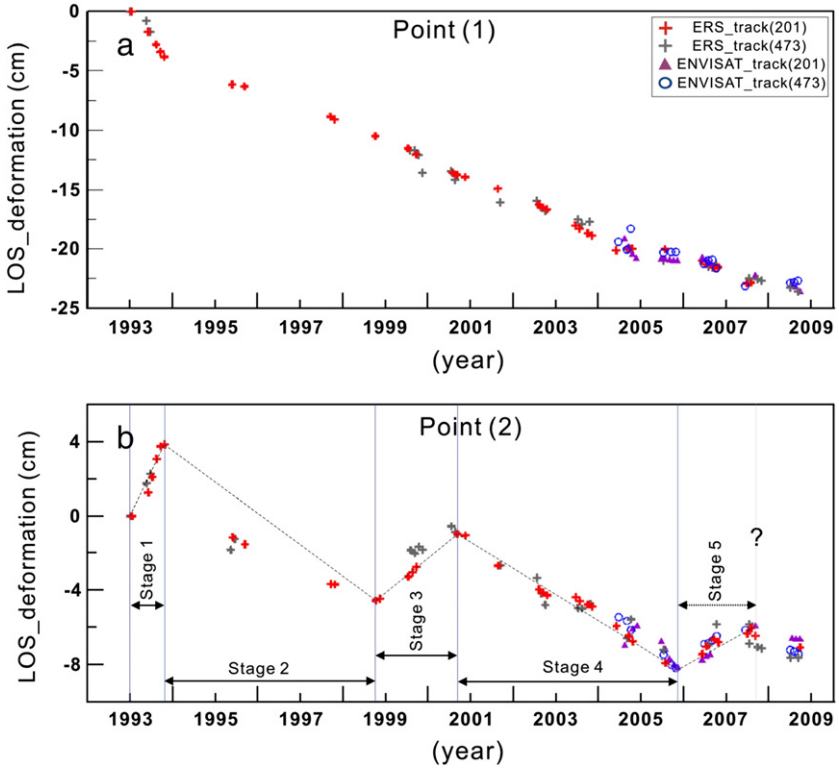

Fig. 5. Surface displacement time-series for (a) a point at the 1977 vent near Pyre Peak on the western caldera of Seguam Island, and (b) a point near the center of the eastern caldera. Time-series results were generated using a refined SBAS processing technique with ERS-1/2 SAR images acquired during 1992–2008 (red and gray crosses) and Envisat images acquired during 2004–08 (blue circles and purple triangles) from tracks 201 and 473, respectively. Locations of points 1 and 2 are shown in Fig. 3.

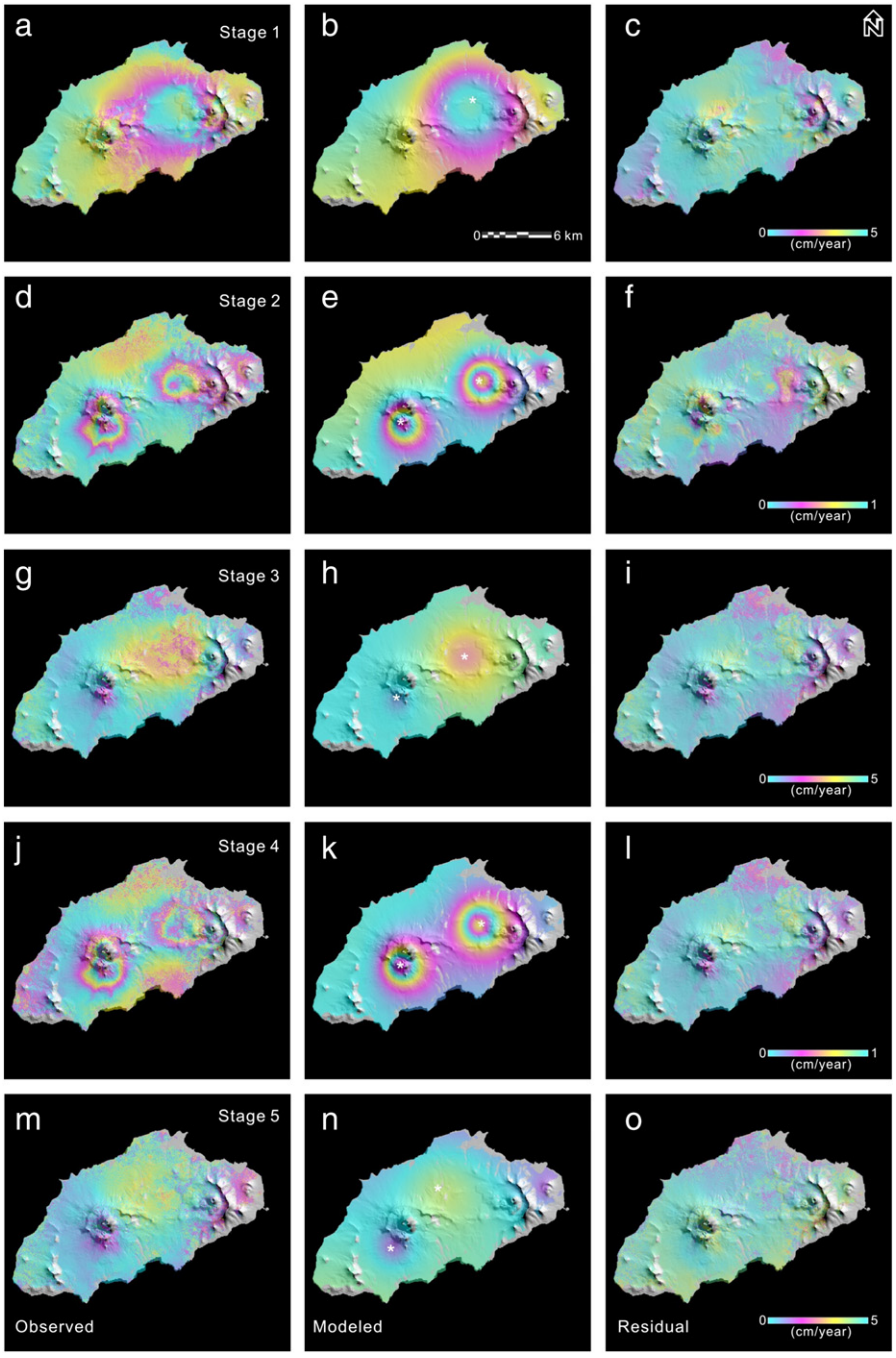

Fig. 6. Average line-of-sight surface displacement rate maps for Seguam during five time intervals (stages) based on the time-series shown in Fig. 5: (a) Stage 1, January 1993–October 1993, (d) Stage 2, October 1993–November 1998, (g) Stage 3, November 1998–September 2000, (j) Stage 4, September 2000–November 2005, and (m) Stage 5, November 2005–July 2007. Images 5b, 5e, 5h, 5k and 5n are corresponding best-fit model interferograms using a Mogi (1958) source with location of source in the center of the caldera (star). Images 5c, 5f, 5i, 5l and 5o are corresponding residual interferograms showing differences between observed and model interferograms.

the best-fit model interferograms shown in Fig. 6b, e, h, k and n. Residual images that show differences between the observed and model interferograms (Fig. 6c, f, i, l and o) are relatively featureless, indicating that Mogi sources fit the observed deformation patterns well. The western deformation source is located ~2 km below sea level (BSL) and contracted at a constant rate of ~1×10^{-4} km^3/year (Table 2). The eastern source is located ~2 km BSL during periods of subsidence (stages 2 and 4) and ~5.5 km BSL during periods of uplift (LOS shortening) (stages 1, 3 and 5). For the eastern source, the contraction rate was 1–2×10^{-4} km^3/year during stages 2 and 4, and the expansion rate was 1–3×10^{-3} km^3/year during stages 1, 3 and 5 (Table 2).

Residual interferograms show that subsidence of both calderas during stages 2 and 4 is modeled well by Mogi sources ~2 km BSL. Agreement between observed and model interferograms of the eastern caldera during periods of uplift (stages 1, 3 and 5) is less satisfactory, so we extended our modeling there to include other types of sources.

3.2. Sill and ellipsoidal models

We used a sill source (Okada, 1985) and a prolate spheroid source (Yang et al., 1988; Fialko and Simons, 2001) to model uplift in the

Table 2
Source parameters for best-fit Mogi sources beneath Seguam Island during 5 deformation stages described in the text.

Western				Eastern			
	Depth (km)	ΔV (km^3/yr)	RMS (mm/yr)		Depth (km)	ΔV (km^3/yr)	RMS (mm/yr)
Stage 1		–		Stage 1	5.5	0.003	6.8
Stage 2	1.8	−0.0001	1.2	Stage 2	2.0	−0.0002	1.3
Stage 3	1.5	−0.00006	1.6	Stage 3	5.0	0.002	3.9
Stage 4	1.9	−0.0001	2.0	Stage 4	1.9	−0.0001	1.8
Stage 5	2.0	−0.0001	1.9	Stage 5	5.2	0.001	1.7

eastern caldera during stages 1, 3 and 5. For the sill source, we computed best-fit estimates of the length, width, depth, strike, dip, and opening of the model sill. For the prolate spheroid source, we estimated lengths of the major and minor axes, depth, strike and dip of the major axis, and pressure change. We slightly filtered the averaged deformation maps from the SBAS processing (Fig. 7a, e, and i). The source parameter estimates derived from modeling the filtered deformation rate images for stages 1, 3 and 5 (Fig. 6b, f, and j) are very similar. For the sill source, the length and width of the sill are ~6.3 km and 6.0–8.4 km, respectively (Table 3). The sill is centered 4.0–5.1 km BSL and opened at a rate of 15–36 mm/year (Table 3; Fig. 7c, g and k). For the prolate spheroid (Yang) source, the lengths of the major and minor axes are ~6 km and 1.5–2.2 km, respectively (Table 4). The spheroidal source is located ~6 km BSL and its internal pressure increased 11.0–81.5 MPa/year, assuming a shear modulus for the host rock of 10 Gpa (Table 4; Fig. 7d,h, and l). The best-fit root-mean-square (RMS) errors for the Mogi, sill, and prolate spheroid sources suggest that the latter two sources fit the observed uplift pattern slightly better than the Mogi source (Tables 2–4). However, the improvement is not statistically significant based on results of

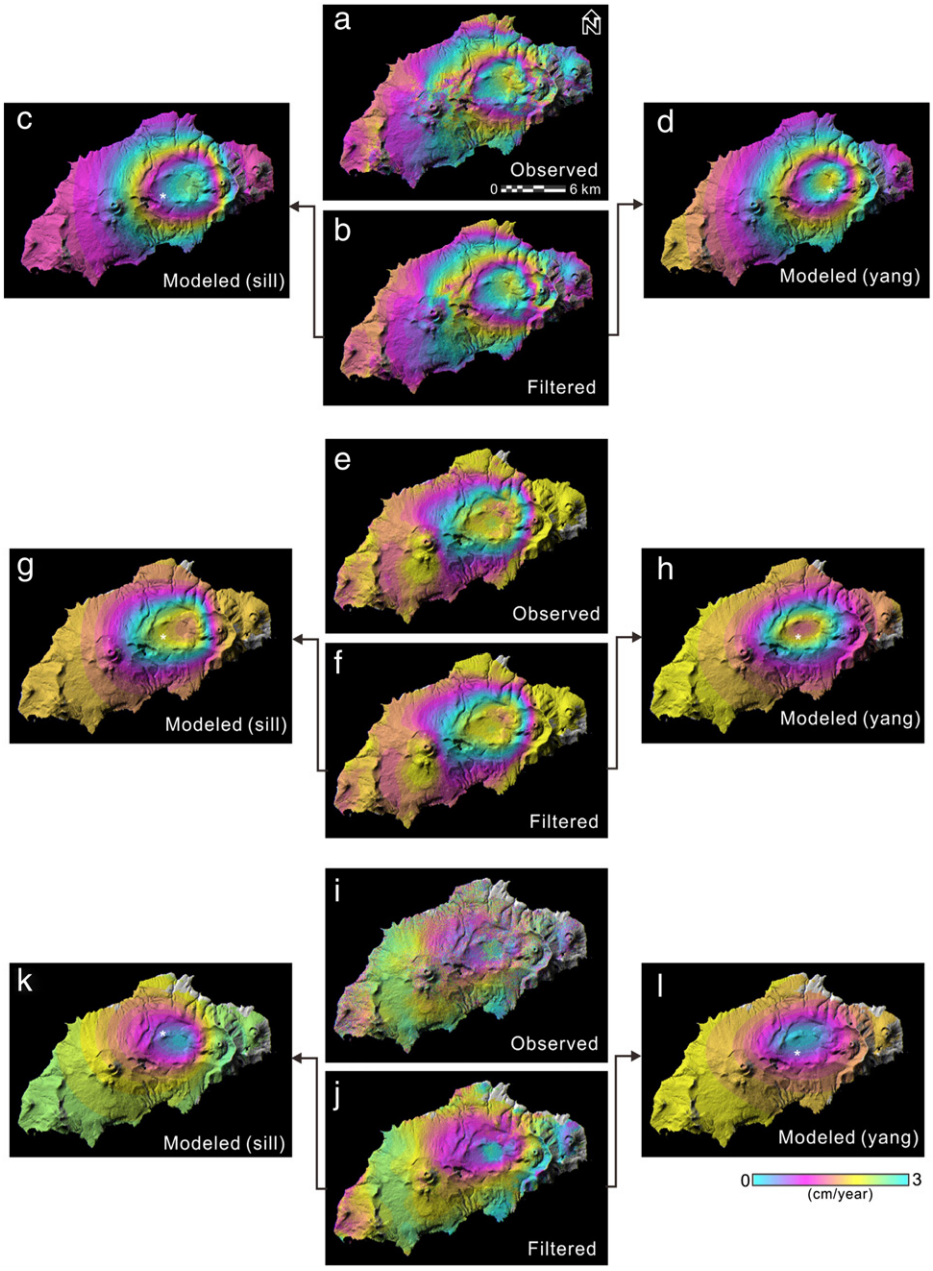

Fig. 7. (a, e and i) Observed average line-of-sight surface displacement rate maps for Seguam volcano during deformation stages 1, 3 and 5, respectively. (b, f and j) Filtered images using observed average images (a, e and i). (c, g and k) Best-fit model results corresponding to b, f and j using a sill source. (d, h and l) Best-fit model results using a prolate spheroid (Yang) source. The star at models represents location of the best fitting sources, respectively.

Table 3
Source parameters for best-fit sill sources beneath the eastern caldera during stages 1, 3 and 5. U3 is sill opening rate.

Eastern caldera							
	Length (km)	Width (km)	Depth (km)	Dip (°)	Strike (°)	U3 (mm/yr)	RMS (mm/yr)
Stage 1	6.3	8.4	5.1	20.1	78.2	36.0	3.7
Stage 3	5.0	8.1	4.0	19.9	80.2	22.0	1.0
Stage 5	5.0	6.0	4.1	0.0	77.9	15.5	3.8

the experimental F-test (Gordon et al., 1987; Dzurisin et al., 2009; Lu et al., 2010).

4. Discussion

Our multi-temporal InSAR analysis using a refined SBAS processing technique identified two distinct deformation sources at Seguam, one beneath each of two calderas. Contraction of the western source resulted in surface subsidence at a constant rate of ~1.6 cm/yr centered near the vents for eruptions in 1977 and 1992–93, and encompassing lava flows from several eruptions during the past few centuries. Based on the location of the source relative to the distribution of 1997 and 1992–93 lava flows (Neal et al., 1996) and the shallow source depth (~2 km BSL), we attribute subsidence in the western caldera at least partly to thermoelastic compaction of young lava flows erupted near Pyre Peak. Subsidence of young lava flows has been observed at other Aleutian volcanoes and attributed to thermoelastic compaction (Lu et al., 2003, 2005, 2010). For example, ongoing subsidence at rates of 1–2 cm/yr has been observed ~50 years after emplacement of lava flows at Okmok volcano (Lu et al., 2005, 2010). Because the modeled source depth (1.5–2.0 km BSL) (Table 2) is much larger than the approximate thickness of the erupted lava flows (tens of meters) (BGVN 02:03), and because the observed subsidence extends outside the 1977 and 1993 lava flows (Figs. 1b versus 6d and j), we interpret that cooling and degassing of magma intruded during past eruptions beneath the western caldera might also play a role in subsidence there (see below).

Deformation of the eastern caldera included alternating periods of uplift caused by a source 2.5–6.0 km BSL and subsidence from a source less than 2 km BSL (Tables 2–4). SBAS InSAR time-series analysis indicates that the uplift source was active episodically while the subsidence source contracted steadily. We are confident that the inflations during stages 1, 3 and 5 were episodic, but less certain whether the subsidence during stages 2 and 4 persisted through the time of the investigation. Because a single inflation source at ~5 km BSL can explain the overall uplift during stages 1, 3 and 5, we could not resolve the subsidence source during the inflation periods. However, it was possible that the subsidence due to the shallower source (~2 km BSL) persisted through the inflation periods. Alternatively, the degassing process stopped during the inflation periods.

We interpret the uplift source at the eastern caldera as an upper crustal magma reservoir identified by Singer et al. (1992) and Jicha and Singer (2006) based on geochemical, petrologic, and isotopic evidence.

Table 4
Source parameters from the best-fit prolate spheroid sources beneath the eastern caldera during stages 1, 3 and 5.

Eastern caldera							
	Major axis (km)	Minor axis (km)	Depth (km)	ΔP (MPa/yr)	Strike (°)	Dip (°)	RMS (mm/yr)
Stage 1	6.0	1.5	6.0	81.5	72.0	46.4	4.0
Stage 3	4.2	2.2	2.6	11.0	78.3	3.0	3.0
Stage 5	4.2	1.5	2.5	12.5	80.0	0.4	4.0

We infer that magma intruded this reservoir episodically to produce the broad uplift patterns observed during stages 1, 3 and 5. We surmise further that cooling and degassing of magma in the upper source of the reservoir contributes to more localized subsidence in the eastern caldera between intrusions. When the magma intrusion rate is low (stages 2 and 4), the net surface displacement subsides. The magma degassing process is efficient such that magma viscosity and density increase dramatically and vertical magma transport stalls at relatively shallow depth (Eichelberger et al., 1986). This pattern mimics what we have observed at other Aleutian volcanoes, notably Akutan (Lu et al., 2000). During stages 1, 3, and 5 when the intrusion rate is greater beneath the eastern caldera (0.001–0.002 km^3/yr or 1–2 km^3/k.y.), surface uplift dominates there. This episodic intrusion rate is consistent with the average eruptive flux at Seguam, 1.2 km^3/k.y. during the past 9 k.y., estimated by Jicha and Singer (2006).

An uplift source beneath the eastern caldera that we interpret as a magma reservoir and the occurrence of all historical eruptions in the western caldera near Pyre Peak is surprising and requires explanation. It is possible that another magma reservoir exists beneath the western caldera and remained static during the period of investigation, which mostly postdates the most recent eruption there, and therefore was not revealed by our analysis. Alternatively, recent eruptions at Seguam might have been fed from a primary reservoir beneath the eastern caldera that sourced the Wilcox Volcano and then survived its collapse 9000 years ago. Lacking geodetic evidence for a second reservoir beneath the western caldera, we speculate that magma from the eastern reservoir episodically migrates laterally toward Pyre Peak along an arc-parallel zone of weakness. That scenario is favored by arc-vertical tectonic extension in the region (Singer et al., 1992; Jicha and Singer, 2006). The existence of the western caldera, which Jicha and Singer (2006) interpret as an explosion feature, suggests that a large volume of magma was erupted from that site at least once in the recent past. Whether that magma was sourced laterally from the eastern reservoir or from an unidentified reservoir beneath the western caldera is not known. If the latter, then cooling and degassing of magma in the western reservoir might contribute to steady subsidence there, as noted above.

We interpret the petrologic evidence provided by Singer et al. (1992) and Jicha and Singer (2006) to mean that Seguam magmas have been sourced from the same reservoir throughout the history of the island. Based on our InSAR results, the reservoir is located 2.5–6.0 km BSL and beneath the eastern caldera of the island. It receives episodic injections of basalt from a deeper source region and reservoir magmas evolve by crystal fractionation through the entire compositional range from basalt to rhyolite. A smaller amount of secondary storage might occur beneath Pyre Peak but petrologic evidence is lacking and geodetic evidence is equivocal (i.e., no observed uplift since 1992 and steady subsidence can be explained otherwise).

5. Conclusion

Eruptions at Seguam are fed from a primary reservoir located 2.5–6.0 km BSL under the eastern caldera of the island in the vicinity of Wilcox Volcano. The reservoir receives episodic injections of basalt from a deeper source, including three injection episodes during the study period resulting in broad surface uplift (January 1993–October 1993, October 1998–September 2000 and November 2005–July 2007). The western caldera of Seguam Island including Pyre Peak, the site of all historical eruptions, subsided steadily throughout the study period mainly as a result of thermoelastic contraction of young lava flows; cooling and degassing of magma intruded to shallow depth (less than 2 km) might also play a role. Alternating periods of subsidence and uplift of the eastern caldera of the island result from steady contraction of a relatively shallow source superimposed on an episodic uplift signal. We attribute steady subsidence to cooling and degassing of the upper source of the magma reservoir and uplift to episodic injections of basalt

into the main body of the reservoir. When magma pressure exceeds the confining strength of the reservoir, it ruptures and magma migrates laterally along a tectonically-favored zone of weakness to erupt at Pyre Peak.

Acknowledgments

This research was supported by the Earth Surface and Interior Program, the USGS Volcano Hazards Program, and the National Institute of Meteorological Research (NIMR 2012-B-3), Korea Meteorological Administration. SAR data used in this study are copyrighted by the European Space Agency (ESA) and were provided by ESA and the Alaska Satellite Facility. We thank C. Wicks for providing the modeling codes, and M. Lisowski and D. George for internal reviews. Any use of trade, product, or firm names is for descriptive purposes only and does not imply endorsement by the U.S. Government.

References

Berardino, P., Fornaro, G., Lanari, R., Sansoti, E., 2002. A new algorithm for surface deformation monitoring based on small baseline differential SAR interferograms. IEEE Transactions on Geoscience and Remote Sensing 40 (11), 2375–2383.

Dzurisin, D., Lisowski, M., Charles, W.W., 2009. Continuing inflation at Three Sisters volcanic center, central Oregon Cascade Range, USA, from GPS, leveling, and InSAR observations. Bulletin of Volcanology 71, 1091–1110.

Eichelberger, J.C., Carrigan, C.R., Westrich, H.R., Price, R.H., 1986. Non-explosive silicic volcanism. Nature 323, 598–602.

Farr, T.G., et al., 2007. The shuttle radar topography mission. Reviews of Geophysics 45, RG2004. http://dx.doi.org/10.1029/2005RG000183.

Ferretti, A., Prati, C., Rocca, F., 2001. Permanent scatterers in SAR interferometry. IEEE Transactions on Geoscience and Remote Sensing 39 (1), 8–20.

Fialko, Y., Simon, M., 2001. Evidence for on-going inflation of the Socorro magma body, New Maxico, from interferometric synthetic aperture radar imaging. Geophysical Research Letters 28 (18), 3549–3552.

Geist, E., Childs, J., Scholl, D., 1987. Evolution of pertroleum geology of Amlia and Amukta intra-arc summit basins, Aleutian ridge. Marine and Petroleum Geology 4, 334–352.

Gonzalez, P.J., Fernandez, J., 2011. Error estimation in multitemporal InSAR deformation time series, with application to Lanzarote, Canary Islands. Journal of Geophysical Research 116, B10404. http://dx.doi.org/10.1029/2011JB008412.

Gordon, R.G., Stein, S., DeMets, C., Argus, D., 1987. Statistical tests for closure of plate motion circuits. Geophysical Research Letters 14, 587–590.

Jicha, B.R., Singer, B.S., 2006. Volcanic history and magmatic evolution of Seguam Island, Aleutian Island arc, Alaska. GSA Bulletin 118, 805–822.

Jicha, B.R., Singer, B.S., Brophy, J.G., Fournelle, J.H., Johnson, C.M., Beard, B.L., Lapen, T.J., Mahlen, N.J., 2004. Variable impact of the subducted slab on Aleutian Island arc magma sources: evidence from Sr, Nd, Pb, and Hf isotopes and trace element abundances. Journal of Petrology 45 (9), 1845–1875.

Lee, C.W., Lu, Z., Jung, H.S., Won, J.S., Dzurisin, D., 2010. Surface deformation of Augustine Volcano (Alaska), 1992–2005, From multiple-interferogram processing using a refined SBAS InSAR approach. USGS Professional Papers, 1769, pp. 453–465.

Lu, Z., Wyss, M., 1996. Segmentation of the Aleutian plate boundary derived from stress direction estimates based on fault plane solutions. Journal of Geophysical Research 101, 803–816.

Lu, Z., Wick, C., Power, J., Dzurisin, D., 2000. Ground deformation associated with the March 1996 earthquake swarm at Akutan volcano, Alaska, revealed by satellite radar interferometry. Journal of Geophysical Research 105 (B9), 21,483–21,495.

Lu, Z., Masterlark, T., Dzurisin, D., Rykhus, R., Wick, C., 2003. Magma supply dynamics at Westdahl volcano, Alaska, modeled from satellite radar interferometry. Journal of Geophysical Research 108 (B7). http://dx.doi.org/10.1029/2002JB002311.

Lu, Z., Masterlark, T., Dzurisin, D., 2005. Interferometric synthetic aperture radar study of Okmok volcano, Alaska, 1922–2003: magma supply dynamics and postemplacement lava flow deformation. Journal of Geophysical Research 110 (B2). http://dx.doi.org/10.1029/2004JB003148.

Lu, Z., Dzurisin, D., Biggs, J., Wicks, C., McNutt, S., 2010. Ground surface deformation patterns, magma supply, and magma storage at Okmok volcano, Alaska, from InSAR analysis: 1. inter-eruptive deformation, 1997–2008. Journal of Geophysical Research 115, B00B03.

Manzo, M., Berardino, P., Bonano, M., et al., 2012. A quantitative assessment of DInSAR time series accuracy in volcanic areas: from the first to second generation SAR sensors. IEEE Inter. Symp. on Geoscience and Remote Sensing IGARSS, pp. 911–914.

Massonnet, D., Feigl, K., 1998. Radar interferometry and its application to changes in the Earth's surface. Reviews of Geophysics 36, 441–500.

Masterlark, T., Lu, Z., 2004. Transient volcano deformation sources imaged with interferometric synthetic aperture radar: application to Seguam Island, Alaska. Journal of Geophysical Research 109. http://dx.doi.org/10.1029/2003JB002568.

Miller, T.P., McGimsey, R.G., Richter, D.H., Riehle, J.R., Nye, C.J., Yount, M.E., Dumoulin, J.A., 1998. Catalog of the historically active volcanoes of Alaska. U. S. Geol. Surv. Open File Rep. 98–0582. (104 pp.).

Mogi, K., 1958. Relations between the eruptions of various volcanoes and the deformations of the ground surfaces around them. Bulletin of the Earthquake Research Institute—University of Tokyo 36, 99–134.

Neal, C.A., McGimsey, R.G., Doukas, M.P., 1996. 1993 volcanic activity in Alaska: summary of events and response of the Alaska Volcano Observatory. U.S. Geological Survey Open-File Report OF 96–0024. (21 pp.).

Okada, Y., 1985. Surface deformation due to shear and tensile faults in a half-space. Bulletin of the Seismological Society of America 75, 1135–1154.

Price, E.J., 2004. Dynamic deformation of Seguam Island, Aleutian Islands, Alaska, 1993–2000: implications for magmatic and hydrothermal processes. Journal of Geophysical Research 109. http://dx.doi.org/10.1029/2003JB002671.

Schmidt, D., Burgmann, R., 2003. Time-dependent land uplift and subsidence in the Santa Clara valley, California, from a large interferometric synthetic aperture radar data set. Journal of Geophysical Research 108 (B9). http://dx.doi.org/10.1029/2002JB002267.

Singer, B.S., Meyers, J.D., Frost, C.D., 1992. Mid-Pleistocene lavas from Seguam volcanic center, central Aleutian arc: closed-system fractional crystallization of a basalt to rhyodacite eruptive suite. Contributions to Mineralogy and Petrology 110 (87-112Zebk).

Williams, C.A., Wadge, G., 1998. The effects of topography on magma chamber deformation models: Application to Mt. Etna and radar interferometry. Geophysical Research Letters 25 (10), 1549–1552.

Yang, X.M., Davis, P.M., Dieterich, J.H., 1988. Deformation from inflation of a dipping finite prolate spheroid in an elastic half-space as a model for volcanic stressing. Journal of Geophysical Research 93 (B5), 4249–4257.